bioRxiv preprint doi: https://doi.org/10.1101/2021.06.03.446862; this version posted August 6, 2021. The copyright holder for this preprint (which was not certified by peer review) is the author/funder, who has granted bioRxiv a license to display the preprint in perpetuity. It is made available under aCC-BY-NC 4.0 International license.

Unrestrained growth of correctly oriented microtubules instructs axonal microtubule orientation

Maximilian AH Jakobs[1,*], Assaf Zemel[2], Kristian Franze[1,3,4,*]

[1] Department of Physiology, Development and Neuroscience, University of Cambridge, Downing Street, Cambridge, CB2 3DY, UK.

[2] Institute of Dental Sciences and Fritz Haber Center for Molecular Dynamics, Hebrew University of Jerusalem, 91120 Jerusalem, Israel.

[3] Institute of Medical Physics, Friedrich-Alexander University Erlangen-Nuremberg, Henkestr. 91, 91052 Erlangen, Germany.

[4] Max-Planck-Zentrum für Physik und Medizin, 91054 Erlangen, Germany

* Correspondence: mj455@cam.ac.uk and kf284@cam.ac.uk

bioRxiv preprint doi: https://doi.org/10.1101/2021.06.03.446862; this version posted August 6, 2021. The copyright holder for this preprint (which was not certified by peer review) is the author/funder, who has granted bioRxiv a license to display the preprint in perpetuity. It is made available under aCC-BY-NC 4.0 International license.

Summary

In many eukaryotic cells, directed molecular transport occurs along microtubules. Within neuronal axons, transport over vast distances particularly relies on uniformly oriented microtubules, whose plus-ends point towards the distal axon tip (+end out). However, axonal microtubules initially have mixed orientations, and what breaks this orientation symmetry is poorly understood. Using live imaging of primary *Drosophila melanogaster* neurons and physical modelling, we found that +end out microtubules surpass a growth transition and undergo persistent long-term growth near the advancing axon tip. In contrast, oppositely oriented microtubules remain short. Using experimental perturbations, we confirmed that the enhanced growth of +end out microtubules is critical for achieving uniform microtubule orientation. Computer simulations of axon development incorporating our data returned +end out microtubules along the entire axonal length, suggesting that the accelerated growth kinetics of correctly oriented microtubules instructs overall axonal microtubule orientation. Our study thus leads to a holistic explanation of how axonal microtubules orient uniformly, a prerequisite for efficient long-range transport essential for neuronal functioning.

bioRxiv preprint doi: https://doi.org/10.1101/2021.06.03.446862; this version posted August 6, 2021. The copyright holder for this preprint (which was not certified by peer review) is the author/funder, who has granted bioRxiv a license to display the preprint in perpetuity. It is made available under aCC-BY-NC 4.0 International license.

Introduction

Symmetry breaking is critical for many biological systems. An organism starts of as a single round cell that divides and differentiates into many cells, tissues and organ systems. The neuron, with its branched dendrites and sometimes exceedingly long axon, is one of the least symmetric cells found in animals. Axons connect neurons with distant targets and thus enable long-distance signal transmission throughout the body at high speed.

The enormous length of axons, which can extend over several meters in some vertebrate species, poses substantial logistical challenges. Proteins and genetic material originating in the cell body need to be actively transported down the axon. Transport occurs along microtubules, which are long, polarized polymers that undergo stochastic cycles of growth and shrinkage (**FIGURE 1A)**. Motor proteins transport cargo either towards a microtubule's dynamic (i.e., growing or shrinking) +end, or the stabilized -end.

In immature axons, microtubule orientation is mixed, with 50-80% of all microtubules pointing with their +end out. During early neuronal development, the fraction of +end out axonal microtubules increases (del Castillo et al., 2015; Yau et al., 2016). In mature axons, ~95% of all microtubules point in the same direction (+end out) (Baas et al., 1989; Heidemann et al., 1981), enabling polarized transport (Millecamps and Julien, 2013). Deficits in polarized transport have been associated with human neurodegenerative diseases, such as Alzheimer's and Parkinson's disease (Millecamps and Julien, 2013). Despite the importance of polarized transport in neuronal axons, the mechanism that breaks microtubule symmetry is still poorly understood.

bioRxiv preprint doi: https://doi.org/10.1101/2021.06.03.446862; this version posted August 6, 2021. The copyright holder for this preprint (which was not certified by peer review) is the author/funder, who has granted bioRxiv a license to display the preprint in perpetuity. It is made available under aCC-BY-NC 4.0 International license.

Microtubules in post-mitotic neurons are not attached to the centrosome (Kuijpers and Hoogenraad, 2011). Nucleation of new microtubules occurs from microtubule organising centres (MTOCs) such as somatic Golgi (Mukherjee et al., 2011) through elongation of severed pieces (Yu et al., 2008) or *de novo* polymerization alongside existing microtubules (Nguyen et al., 2014; Sánchez-Huertas et al., 2016). These newly formed microtubules often orient in the same direction as existing ones, enforcing any pre-existing orientation bias (Mattie et al., 2010; Mukherjee et al., 2020), which by itself cannot explain the +end out orientation of microtubules in mature axons. Furthermore, in axons, short microtubules pointing with their -end out can be transported towards the cell body (i.e., away from the tip) by cytoplasmic dynein, a process likely assisted by the microtubule bundling protein TRIM46 (del Castillo et al., 2015; Rao et al., 2017; van Beuningen et al., 2015). However, also this mechanism is not sufficient to explain how axonal microtubules orient with their +ends pointing away from the cell body (see below).

Results

Correctly oriented microtubules add more length per growth cycle

To address how microtubule orientation in neuronal axons is achieved, we cultured acutely dissociated neurons from the *Drosophila melanogaster* larval CNS (Egger et al., 2013). To quantify microtubule growth in axons, we crossed *Drosophila* lines expressing the fusion protein EB1-GFP, which labels growing microtubule +ends with bright 'comets' (**FIGURE 1A-C**) (Stepanova et al., 2003). The distance over which a comet moves in the axon is equal to the overall length d_g that

bioRxiv preprint doi: https://doi.org/10.1101/2021.06.03.446862; this version posted August 6, 2021. The copyright holder for this preprint (which was not certified by peer review) is the author/funder, who has granted bioRxiv a license to display the preprint in perpetuity. It is made available under aCC-BY-NC 4.0 International license.

is added to a microtubule between the start of its growth cycle and the catastrophe leading to microtubule shrinkage (**FIGURE 1A)**. The direction of growth highlights whether a microtubule is oriented with its +end away from (+end out) or towards (-end out) the cell body. Time-lapse movies of EB1-GFP comets were converted into kymographs and analyzed using *KymoButler* (Jakobs et al., 2019) (**FIGURE 1C-D**).

The fraction of +end out microtubules increased over time and with increasing axonal length (**SUPPLEMENTARY FIGURE 1**), confirming that microtubule orientation increases during development (del Castillo et al., 2015; Yau et al., 2016). Most microtubule growth events (~66%) were found within the first 20 µm from the advancing axon tip (**FIGURE 1A,E**). Microtubule growth lengths per cycle, d_g , were significantly higher near the axon tip compared to further away from it (**FIGURE 1F**). Furthermore, +end out microtubules added significantly more length per growth cycle than -end out microtubules, with the highest difference between +end out and -end out microtubules (~0.5 µm/cycle) found within the first 10 µm from the axon tip (**FIGURE 1G**). Hence, the orientation of microtubules that added more length per growth cycle (i.e., +end out microtubules) became the dominant microtubule orientation during neuronal development, indicating a correlation between increased +end out microtubule growth and the fraction of +end out microtubules in axons.

Enhanced growth of +end out microtubules leads to unbounded growth

bioRxiv preprint doi: https://doi.org/10.1101/2021.06.03.446862; this version posted August 6, 2021. The copyright holder for this preprint (which was not certified by peer review) is the author/funder, who has granted bioRxiv a license to display the preprint in perpetuity. It is made available under aCC-BY-NC 4.0 International license.

On long time scales, differences in microtubule growth length per growth cycle should primarily affect average microtubule lengths l_{MT}. To test whether the rather small differences in d_g of ~0.5 µm/cycle lead to biologically meaningful differences in the average expected microtubule lengths between +end out and -end out oriented microtubules, we formulated a 2-state Master equation model of microtubule growth and shrinkage (see (Dogterom and Leibler, 1993) & supplemental methods for details The model distinguishes two regimes (**FIGURE 2A**):

$$l_{MT} = \begin{cases} d_g d_s/(d_s - d_g) & d_s > d_g \quad \text{('bounded' growth)} \\ \infty & d_s \leq d_g \quad \text{('unbounded' growth)} \end{cases} \tag{1}$$

where d_s = lost length per shrinkage cycle.

When $d_s \leq d_g$, the average length added to the microtubule exceeds the average shrinkage length per cycle so that a microtubule will exhibit net growth and elongate as long as physically possible in its confined environment (called 'unbounded' growth). For $d_s > d_g$, however, growth is 'bounded' and average microtubule lengths follow an exponential distribution with a mean of $d_s d_g/(d_s - d_g)$. In practice, this means that microtubules with $d_g \geq d_s$ would grow until encountering a physical barrier (for example the axon tip), while microtubules with $d_s > d_g$ remain finite (approximately 2 µm with d_s = 2.2 µm and d_g = 1 µm).

We determined the microtubule shrinkage per cycle d_s by co-expressing a Jupiter-mCherry fusion protein (a tubulin marker) together with EB1-GFP in *D. melanogaster* axons. Microtubules stopped growing when the GFP signal disappeared from their +end, indicating a catastrophe event. Subsequent microtubule shrinkage was visualized by simultaneously imaging tubulin (Jupiter-mCherry), and quantified by tracing the resulting tubulin edges in the dual colour

bioRxiv preprint doi: https://doi.org/10.1101/2021.06.03.446862; this version posted August 6, 2021. The copyright holder for this preprint (which was not certified by peer review) is the author/funder, who has granted bioRxiv a license to display the preprint in perpetuity. It is made available under aCC-BY-NC 4.0 International license.

kymographs (**FIGURE 2B-D**). Axonal microtubule shrinkage lengths were d_s = 2.2 ± 0.2 µm / cycle (mean ± s.e.m., **FIGURE 2E**). With this value for d_s, our model predicted the divergence of l_{MT} at around d_g = 2.2 µm (**FIGURE 2F).** The measured values of d_g *and* d_s hence suggested that +end out-oriented microtubules within 10 µm from the axon tip exhibit a considerably higher likelihood of unbounded growth than -end out microtubules within that range and any microtubule further away from the tip (**FIGURE 2F)**. The enhanced growth of +end out microtubules near the axon tip implied a higher chance of survival for +end out microtubules while leaving -end out microtubules labile, thus establishing and maintaining overall axonal +end out microtubule orientation.

Enhanced growth of +end out microtubules is required for uniform microtubule orientation

To test this hypothesis, we decreased microtubule growth using Nocodazole, a drug that disrupts microtubule polymerization. We also decreased microtubule growth by increasing the osmolarity of the cell culture medium (BRAY et al., 1991; Molines et al., 2020), potentially by decreasing the space for microtubules to polymerize into (Franze, 2020). In both approaches, axons exhibited significantly decreased +end out microtubule growth at the axon tip (< 10 µm), with d_g < 1.7µm / cycle (**FIGURE 3A-E**). In agreement with our prediction, microtubules within these axons were overall significantly less uniformly oriented (**FIGURE 3D-E**), confirming an important role of the enhanced growth lengths per cycle of +end out microtubules in establishing axonal microtubule orientation.

bioRxiv preprint doi: https://doi.org/10.1101/2021.06.03.446862; this version posted August 6, 2021. The copyright holder for this preprint (which was not certified by peer review) is the author/funder, who has granted bioRxiv a license to display the preprint in perpetuity. It is made available under aCC-BY-NC 4.0 International license.

p150 protein gradient in axon tips promotes enhanced microtubule growth

However, why do +end out microtubules grow longer in the vicinity of the axon tip? Local gradients of microtubule growth-promoting factors could lead to an increase in +end microtubule growth in that region (**FIGURE 1G**). Axon tips contain a multitude of different proteins and are the site of protein synthesis (Lowery and Van Vactor, 2009). Locally synthesized microtubule growth-promoting factors include microtubule stabilizing proteins, such as p150 (Lazarus et al., 2013; Moughamian and Holzbaur, 2012), CRMP-2 (Fukata et al., 2002; Inagaki et al., 2001), and TRIM46 (Rao et al., 2017; van Beuningen et al., 2015), as well as free tubulin and others (Eng et al., 1999).

Drosophila has a p150 homologue which, similar to murine neurons (Moughamian and Holzbaur, 2012), is enriched in axon (but not in dendritic) tips (**FIGURE 3F, H AND SUPPLEMENTARY FIGURE 2**). These dendritic processes exhibited no +end out microtubule orientation (**SUPPLEMENTARY FIGURE 3**). Inserting the measured axonal p150 gradient profile into a mathematical model indicated that the observed gradient should, in theory, be able to cause different growth behaviours for +end out and -end out microtubules in axonal tips (**SUPPLEMENTARY FIGURE 4**). Accordingly, +end out microtubule growth lengths per cycle d_g were significantly higher in axons than in dendritic processes -which exhibited mixed microtubule polarities (**SUPPLEMENTARY FIGURE 3**).

To test this prediction further, we assessed microtubule dynamics in *wild-type*, *p150-RNAi* expressing neurons, and in neurons from $p150^1$/+ mutant flies (**FIGURE 3G-K**). $p150^1$ (also known as Gl^1) mutants express a truncated p150-RNA transcript, which results in a dominant negative phenotype (Plough and Ives, 1935). Both the expression of *p150-RNAi* and of dominant negative $p150^1$/+ led to a significant decrease in +end out microtubule growth within 10 µm from the axon

bioRxiv preprint doi: https://doi.org/10.1101/2021.06.03.446862; this version posted August 6, 2021. The copyright holder for this preprint (which was not certified by peer review) is the author/funder, who has granted bioRxiv a license to display the preprint in perpetuity. It is made available under aCC-BY-NC 4.0 International license.

tip (**FIGURE 3L**). In agreement with our model, microtubule orientation was significantly decreased in both *p150-RNAi* and *p150^{1}/+* axons compared to controls (**FIGURE 3M**), indicating that growth-promoting protein gradients at the axon tip do indeed have an important role in regulating the overall polarization of the axonal microtubule network.

Kinesin 1 is required to establish p150 gradient

Previous work showed that p150 accumulation at axon tips depends on the activity of the microtubule-specific molecular motor protein kinesin 1 (Moughamian and Holzbaur, 2012; Twelvetrees et al., 2016), which preferentially enters axons over dendrites (Tas et al., 2017). Accordingly, disruption of kinesin 1 function with an RNAi treatment led to considerable mislocation of p150 along axons (**SUPPLEMENTARY FIGURE 5A-D**). Again, the absence of a p150 gradient in these neurons led to significantly decreased +end out microtubule growth near the axon tip, and hence to an overall decrease in axonal microtubule orientation (**SUPPLEMENTARY FIGURE 5E-I**).

Uniform axonal microtubule polarity is established through a combination of microtubule sliding, templating, and unbounded growth

In addition to unbounded +end out microtubule growth identified here, other mechanisms have previously been suggested to be involved in regulating the overall axonal microtubule orientation, including dynein-mediated sliding of -end out microtubules towards the cell body (del Castillo et

bioRxiv preprint doi: https://doi.org/10.1101/2021.06.03.446862; this version posted August 6, 2021. The copyright holder for this preprint (which was not certified by peer review) is the author/funder, who has granted bioRxiv a license to display the preprint in perpetuity. It is made available under aCC-BY-NC 4.0 International license.

al., 2015; Rao et al., 2017) and augmin-mediated microtubule templating, that is nucleating microtubules tend to have the same orientation as existing ones in the same cellular region) (Nguyen et al., 2014; Sánchez-Huertas et al., 2016). To investigate the role of these mechanisms and the enhanced microtubule growth identified in this study in establishing the axonal microtubule polarity, we used computer simulations.

When we implemented microtubule sliding and/or templating as the only mechanisms of microtubule sorting, simulations returned a steady state in which a fixed fraction of the axon length close to the cell body remained enriched with -end-out microtubules (**Figure 4A,B and Supplementary Figure 6**), in disagreement with experimental findings (Yau et al., 2016) (**Figure 4D)**. Similarly, the unbounded growth of +end out microtubules alone (**Supplementary Figure 6C**) also failed to capture the high fractions of +end out microtubules observed experimentally at the axon entry (**Figure 4B**). However, integrating sliding, templating, and unbounded +end out microtubule growth in the simulation (assuming that the likelihood of exhibiting unbounded growth corresponds to a successful nucleation event) led to axons with +end out microtubule orientation all along their length, recapitulating our experimental results (**Figure 4C-D and Supplementary Figure 6**). This highlights the necessity of multiple mechanisms to establish and maintain axonal microtubule orientation. Similarly, a combination of different microtubule growth-promoting proteins (e.g., tubulin, TRIM46, CRMP2, and/or p150) is likely to contribute to unbounded microtubule growth into the axon tip.

Discussion

bioRxiv preprint doi: https://doi.org/10.1101/2021.06.03.446862; this version posted August 6, 2021. The copyright holder for this preprint (which was not certified by peer review) is the author/funder, who has granted bioRxiv a license to display the preprint in perpetuity. It is made available under aCC-BY-NC 4.0 International license.

We here found that an enrichment of microtubule growth-promoting proteins at the advancing axon tip leads to a transition of microtubule growth from a bounded to an unbounded state. This growth transition is an essential requirement for the establishment of the uniform +end out microtubule orientation found in mature axons. While previous studies suggested that microtubule dynamics are temporally and spatially constant during early axon formation (Seetapun and Odde, 2010), our results suggest that, at later stages of axon maturation, microtubule dynamics are heterogeneous (**FIGURE 1**).

p150, which we investigated here as an example growth-promoting protein, was concentrated at axon tips but was not enriched at dendritic tips (**SUPPLEMENTARY FIGURE 2).** Enhanced growth of +end out microtubules essential for establishing uniform microtubule orientation was only observed near axonal but not near dendritic tips (**SUPPLEMENTARY FIGURE 3**), confirming that differences in the localization of microtubule growth-promoting proteins correlate with differences in microtubule growth. Perturbations of p150 led to decreased +end out microtubule growth in the axon tip and thus to decreased overall microtubule order in the axon (**FIGURE 3**).

p150 is mainly known for of its role in the dynactin complex, which is an important cargo adapter protein for the molecular motor protein dynein (Gill et al., 1991). Since p150 and dynein are functionally related, it is difficult to separate their individual contributions to microtubule growth and cell body-directed sliding of -end out microtubules. However, it remains unclear whether p150 is required for dynein-mediated microtubule sliding (Ahmad et al., 1998; Waterman-Storer et al., 1997), and the *Drosophila melanogaster* oocyte also contains a biased microtubule cytoskeleton whose orientation is, presumably, maintained by p150 (Nieuwburg et al., 2017).

bioRxiv preprint doi: https://doi.org/10.1101/2021.06.03.446862; this version posted August 6, 2021. The copyright holder for this preprint (which was not certified by peer review) is the author/funder, who has granted bioRxiv a license to display the preprint in perpetuity. It is made available under aCC-BY-NC 4.0 International license.

Hence, while p150 is unlikely to induce unbounded microtubule growth alone, it emerges as a key contributor to the establishment of microtubule orientation.

In addition to its contribution to the p150 gradient in axon tips (**Supplementary Figure 5**), kinesin 1 is also thought to slide microtubules with their -end leading (del Castillo et al., 2015). Kinesin knockdown should thus decrease the number of -end out microtubules sliding into the distal axon. Instead, we observed that disruption of kinesin 1 function led to an increase in the fraction of -end out microtubules in the distal axon (**Supplementary Figure 5**), suggesting that kinesin 1 affects microtubule orientation mainly via localising p150 or other microtubule growth or nucleation promoting proteins (e.g., CRMP-2 or MTOCs such as gammaTubulin) to axonal tips.

Furthermore, both kinesin 1 and p150/dynactin perturbations could potentially also affect MTOC localization in neurons. p150 was enriched at the tips of axonal but not of dendritic processes (**Supplementary Figure 2**). In *C. elegans* neurons, MTOCs may be located to the tips of dendritic processes (Liang et al., 2020). Removal of dynactin, which initiates cell body-directed transport from axonal tips (Moughamian and Holzbaur, 2012), could lead to an increased number of MTOCs also at axon tips, thereby promoting growth and nucleation of microtubules. However, our results showed a decrease in microtubule growth dynamics at axon tips after dynactin removal (**Figure 3**), indicating that the observed decrease in microtubule orientation was mostly due to decreased rather than promoted growth of axonal microtubules in the axon tip.

We propose the following model explaining the spontaneous establishment of microtubule orientation in developing axons. Growth-promoting proteins accumulate at the axon tip due to microtubule +end-directed transport by kinesin motors (**Supplementary Figure 5**). The resulting

bioRxiv preprint doi: https://doi.org/10.1101/2021.06.03.446862; this version posted August 6, 2021. The copyright holder for this preprint (which was not certified by peer review) is the author/funder, who has granted bioRxiv a license to display the preprint in perpetuity. It is made available under aCC-BY-NC 4.0 International license.

protein gradient leads to a local bias in microtubule growth (**FIGURE 1**, **FIGURE 3**), rendering +end out microtubule growth into the axon tip unbounded (**FIGURE 2**). In contrast, short -end out microtubules are more prone to depolymerization and/or transport away from the tip by dynein-mediated cell body-directed sliding (del Castillo et al., 2015; Yau et al., 2016), thus contributing to the orientation bias of microtubules in the axon. This bias is further enhanced by augmin-mediated templating to establish and maintain a fully organized microtubule cytoskeleton (see **FIGURE 4E** for a schematic summary). Together with cell process length-dependent microtubule accumulation (Seetapun and Odde, 2010), these mechanisms cooperate to build the polarized microtubule network that enables efficient long-range transport in neuronal axons. Future work will reveal whether other cellular systems use similar mechanisms to organize their cytoskeleton.

bioRxiv preprint doi: https://doi.org/10.1101/2021.06.03.446862; this version posted August 6, 2021. The copyright holder for this preprint (which was not certified by peer review) is the author/funder, who has granted bioRxiv a license to display the preprint in perpetuity. It is made available under aCC-BY-NC 4.0 International license.

Materials and Methods

Key Resource Table

Reagent or Resource	Source	Identifier
Experimental Models: Organisms/Strains		
D. melanogaster: EB1-GFP	(Bulgakova et al., 2012)	N/A
D. melanogaster: ubi EB1-GFP	(Shimada et al., 2006)	N/A
D. melanogaster: Jupiter-mcherry	(Bergstralh et al., 2015)	N/A
D. melanogaster: p150^{1}	Bloomington	RRID:BDSC_504
D. melanogaster: p150-RNAi	Bloomington	RRID:BDSC_3785
D. melanogaster: khc-RNAi	Bloomington	RRID:BDSC_35770
D. melanogaster: elav-gal4	Bloomington	RRID:BDSC_458
Antibodies		

bioRxiv preprint doi: https://doi.org/10.1101/2021.06.03.446862; this version posted August 6, 2021. The copyright holder for this preprint (which was not certified by peer review) is the author/funder, who has granted bioRxiv a license to display the preprint in perpetuity. It is made available under aCC-BY-NC 4.0 International license.

Rb anti-p150	(Nieuwburg et al., 2017)	N/A
Ms anti-alpha-tubulin	Abcam	Cat#: ab7291 RRID:AB_2241126
Celltracker™	Invitrogen	Cat#: C2925
CF633 anti-Rb	Cambridge Bioscience	Cat#: BT20125
AF405 anti-Ms	Thermo Fisher	Cat#: ab175658 RRID:AB_2687445

Software and Algorithms

MATLAB	Mathworks	RRID:SCR_001622
Mathematica	Wolfram	RRID:SCR_014448
KymoButler	(Jakobs et al., 2019)	https://gitlab.com/ deepmirror/kymobutler
ImageJ	(Schindelin et al., 2012)	RRID:SCR_003070
Neurite Tracer	(Pool et al., 2008)	RRID:SCR_016566

bioRxiv preprint doi: https://doi.org/10.1101/2021.06.03.446862; this version posted August 6, 2021. The copyright holder for this preprint (which was not certified by peer review) is the author/funder, who has granted bioRxiv a license to display the preprint in perpetuity. It is made available under aCC-BY-NC 4.0 International license.

Fly stocks

Microtubule +end dynamics were visualized with a transgenic fly line expressing EB1-GFP heterozygously under its endogenous promoter (*wh;+;eb1-gfp/tm6b,* gift from the Brown laboratory in Cambridge) (Bulgakova et al., 2013) or a fly expressing EB1-GFP under a *ubiquitin* promotor (*ubi:eb1-gfp;+;+,* gift from the St. Johnston laboratory in Cambridge) (Shimada et al., 2006). Whole microtubules were labelled with Jupiter-mcherry (*wh;if/cyo;Jupiter-mcherry*, gift from the St. Johnston laboratory in Cambridge) (Bergstralh et al., 2015). Other stocks used: *p150*^{1} (Bloomington # 504)*, uas:p150-RNAi* (Vienna Drosophila Stock Center # 3785), *uas:khc-RNAi* (Bloomington # 35770), *khc27* (Bloomington # 67409), khc17 (gift from the St. Johnston laboratory in Cambridge). *uas* constructs were driven by *elav-gal4* (Bloom# 458, *elav* is a neuron specific promotor that ensures the construct is only expressed in the CNS (Yannoni and White, 1997)) and transgenic lines were generated through standard balancer crossing procedures.

Primary cell culture

3rd instar larvae were picked, and their CNS dissected similarly to (Egger et al., 2013; Sanchez-Soriano et al., 2010). As described in (Egger et al., 2013) the resulting primary culture comprised a mixture of terminally differentiated larvae neurons such as peripheral neurons alongside precursors cells and immature neurons of the adult fly brain. Thereby, the larval CNS lends itself to the study of a heterogenous population of neurons. The CNS tissue was homogenized and dissociated in 100 µl of Dispersion medium (Hank's Balanced Salt Solution (1xHBSS, Life Technologies, 14170088) supplemented with Phenylthiourea (Sigma-Aldrich P7629, 0.05mg/ml), Dispase (Roche 049404942078001, 4mg/ml), and Collagenase (Worthington Biochem. LS004214,

bioRxiv preprint doi: https://doi.org/10.1101/2021.06.03.446862; this version posted August 6, 2021. The copyright holder for this preprint (which was not certified by peer review) is the author/funder, who has granted bioRxiv a license to display the preprint in perpetuity. It is made available under aCC-BY-NC 4.0 International license.

1mg/ml)) for 5 minutes at 37°C. The media was topped up with 200 µl of Cell Culture Medium (Schneider's Medium, Thermo Fisher 21720024) supplemented with insulin (2 µg/ml Sigma I0516) and fetal bovine serum (1:5 Thermo Fisher Scientific A3160801)) and cells were spun down for 6 min at 650 rcf. The pellet was resuspended in Cell Culture Medium at 5 brains/120 µl. Cells were grown at 26°C for 1.5 hours in a droplet of 30 µl Cell Culture Medium in a glass bottom dish between the coated glass and an uncoated glass slide on top. Initially the cells were cultured with the coated coverslip facing down. After 1.5 hours the chambers were flipped so that cells that did not attach floated off to the opposite (uncoated) side. Culture times were: 4-26 hours (for measuring microtubule orientation profiles in short and long axons), 22-26 hours (for measuring microtubule dynamics, both Patronin-YFP and EB1-GFP), and 22-48 hours (for measuring microtubule dynamics in dendritic processes).

To measure the effect Nocodazole has on microtubule orientation in axons, the medium was supplemented with 5uM of Nocodazole (Dissolved in DMSO, Sigma-Aldrich M1404-2MG) w approximately 12h post-plating and 12h before measuring microtubule dynamics. The control cells were treated with 0.025% DMSO in culture medium. Treatment and corresponding controls were always run in parallel, and when possible, from the same fly stock. *Uas* driven overexpression was controlled with a fly expressing both *elav::gal4* and *eb1-gfp* to control for the expression of gal4 protein.

To measure the effects of osmolarity changes in the surrounding medium we increased the osmolarity of the culture medium by approximately 100 mOsm by adding 4g NaCl. Cells were first cultured in normal media for 1.5h. Subsequently, the media was removed and replaced with

bioRxiv preprint doi: https://doi.org/10.1101/2021.06.03.446862; this version posted August 6, 2021. The copyright holder for this preprint (which was not certified by peer review) is the author/funder, who has granted bioRxiv a license to display the preprint in perpetuity. It is made available under aCC-BY-NC 4.0 International license.

either fresh media (control) or media supplemented with 4g NaCl. Cells were again imaged after 22-26h post plating.

Live imaging of microtubules

All live imaging movies were acquired on a Leica DMi8 inverted microscope with a 63x objective (oil immersion, NA=1.4, Hamamatsu Orca Flash 2.0 camera) and at room temperature (22-25°C). To reduce autofluorescence during imaging, the culture medium was replaced with Live Imaging Solution (Thermo Fisher A14291DJ). Culture media was not replaced for imaging cells in Nocodazole, DMSO, and osmo+ to enable measurement of microtubule dynamics in the chosen media. For EB1-GFP imaging, an image (exposure time 500 ms) was taken every 2 seconds for 70-150 frames depending on sample bleaching. When imaging both EB1-GFP and Jupiter-mcherry simultaneously, one image was taken every 3 seconds for 100 frames (exposure 500ms). Lamp intensity was set to the lowest level that enabled visual identification of labels.

p150 antibody staining

24 hours after plating, the cells were treated with 5µM of Celltracker™ (Invitrogen C2925) dye for 30 minutes to label cells in green. Subsequently, cells were fixed in pre-warmed 4% paraformaldehyde (PFA) (pH 7.2, 26°C) for 50 minutes. Post-fixation, the cells were washed in PBS once and then incubated with mouse alpha-tubulin 1:1000 (Abcam ab7291) and rabbit glued/p150 antibody 1:500 (gift from the St Johnston laboratory, (Nieuwburg et al., 2017)) diluted in PBST (2x phosphate-buffered saline (PBS, Oxoid BR0014G) tablets in 400ml H2O + 1.2 ml Triton X-100) + 0.01 g/ml bovine serum albumin at 4°C overnight (~14h). After two quick

bioRxiv preprint doi: https://doi.org/10.1101/2021.06.03.446862; this version posted August 6, 2021. The copyright holder for this preprint (which was not certified by peer review) is the author/funder, who has granted bioRxiv a license to display the preprint in perpetuity. It is made available under aCC-BY-NC 4.0 International license.

washes in PBS, the cells were incubated with the secondary antibodies Alexa Fluor 647 (far-red, Thermo Fisher A-21236) and 405 (blue, Thermo Fisher A-31556) for 1.5 hours at room temperature. After another two quick PBS washes, the cells were mounted in Fluoromount (Thermo Fisher 00-4958-02) and imaged.

Images were analyzed by drawing a line along axon processes from the base of the axon to its tip in the tubulin channel. The intensity profiles for all 3 channels (p150, tubulin, and Celltracker) were extracted and normalized by their respective median values, and the p150 channel was normalized to the Celltracker channel. Finally, the *p150-RNAi* p150 profiles were normalized by their respective *wild-type* control. The resulting profiles (per axon) were then pooled over all biological replicates, binned in 10 µm wide bins, and plotted in *Mathematica*.

EB1-GFP dynamics

Kymographs of EB1-GFP tracks in *Drosophila melanogaster* axons were generated by first using the Neurite Tracer plugin in ImageJ to draw lines along axons or dendrites from the centre of the cell body to the farthest EB1-GFP comet signal, i.e. the distalmost growth event (Pool et al., 2008). Subsequently a custom *Mathematica* (https://wolfram.com) algorithm automatically generated kymographs from these lines by plotting the average pixel intensity of 3 adjacent pixels into rows of an image for each frame. The resulting image was then smoothed with a Gaussian kernel of size 3 and wavelet filtered to remove noise. Kymographs were analyzed with *KymoButler* and subsequently post processed in *MATLAB* (https://mathworks.com). Tracks were removed in case: (i) they displaced less than 2 pixels along the x-axis, (ii) they were slower than 1.5 µm/min, (iii) they were faster than 20 µm/min, and (iv) they were visible for less than 4 frames. Additionally,

bioRxiv preprint doi: https://doi.org/10.1101/2021.06.03.446862; this version posted August 6, 2021. The copyright holder for this preprint (which was not certified by peer review) is the author/funder, who has granted bioRxiv a license to display the preprint in perpetuity. It is made available under aCC-BY-NC 4.0 International license.

control experiments and their corresponding treatment condition were discarded if the control axons exhibited a mean orientation below 0.8 or average growth velocities below 2 µm/min. To account for outlier comets, the distance from the axon tip was calculated as the distance from the 0.95 quantile EB1-GFP comet.

Note that, mature *D. melanogaster* dendrites *in vivo* exhibit a mixed microtubule orientation (Stone et al., 2008). However, we cultured neurons only up to 48h which might be too short to form fully developed dendrites and our minimal cell culture medium is likely lacking growth factors that would enable further differentiation to form fully -end out dendrites. Additionally, vertebrate dendrites also appear to acquire their characteristic orientation over time (Baas et al., 1989).

Jupiter-mcherry & EB1-GFP

Kymographs were prepared as for imaging EB1-GFP only (i.e. using Neurite Tracer). Individual shrinkage events were extracted by hand from the resulting kymographs using the ROI tool in *ImageJ* (https://imagej.net). The tracks were then analyzed and plotted with *MATLAB* and *Mathematica*. Measuring microtubule shrinkage dynamics was only possible in regions of low tubulin content, e.g., near the axon tip. We implicitly assumed that microtubule shrinkage depends neither on microtubule orientation nor on its position along the axon. However, experimental evidence suggests that a decrease in microtubule growth length correlates with an increase in shrinkage length (Vasquez et al., 2017), indicating that we likely overestimated microtubule lengths further away from the axon tip, therefore underestimating the difference between +end out microtubules at the tip and those further away from it.

bioRxiv preprint doi: https://doi.org/10.1101/2021.06.03.446862; this version posted August 6, 2021. The copyright holder for this preprint (which was not certified by peer review) is the author/funder, who has granted bioRxiv a license to display the preprint in perpetuity. It is made available under aCC-BY-NC 4.0 International license.

Statistics

For comparing two groups the Wilcoxon rank sum test was used as implemented in MATLAB (https://www.mathworks.com/help/stats/ranksum.html). The standard error of the mean (s.e.m.) was calculated as $s.e.m. = \sigma/\sqrt{n}$. Here σ is the standard deviation of the sample and n is the number of samples. We used the Kruskal Wallis test (https://uk.mathworks.com/help/stats/kruskalwallis.html) to compare several samples, followed by a Dunn Sidak post hoc test.

Solution of the 2-state master equation

We assumed that microtubules are able to either grow or shrink, and each of these two states (g and s in short) has a probability distribution that depends on microtubule length l and time t ($p_g(l,t)$ and $p_s(l,t)$). Microtubules can furthermore stop growing and start shrinking with rate $f_g = 1/t_g$ (t_g being the average microtubule growth time) and stop shrinking to start growing with rate $f_s = 1/t_s$ (t_s being the average microtubule shrinkage time). Furthermore, microtubules are assumed to grow with velocity v_g and shrink with velocity v_s, while they are in the growing- or shrinking- state, respectively. Writing this as a master equation yields:

$$\frac{\partial}{\partial t} p_s(l,t) = f_g\, p_g(l,t) - f_s\, p_s(l,t) + v_s \frac{\partial}{\partial l} p_s(l,t)$$

$$\frac{\partial}{\partial t} p_g(l,t) = f_s\, p_s(l,t) - f_g\, p_g(l,t) - v_g \frac{\partial}{\partial l} p_g(l,t)$$

To solve this set of partial differential equations consider the following Fourier transformation of $p_s(l,t)$ and $p_g(l,t)$:

bioRxiv preprint doi: https://doi.org/10.1101/2021.06.03.446862; this version posted August 6, 2021. The copyright holder for this preprint (which was not certified by peer review) is the author/funder, who has granted bioRxiv a license to display the preprint in perpetuity. It is made available under aCC-BY-NC 4.0 International license.

$$p_{s,g}(l,t) = \int dk\, d\omega\; e^{i\omega t - ikl}\, \tilde{p}_{s,g}(\omega,k)$$

Substituting in the 2-state master equation yields:

$$0 = \int dk\, d\omega\, e^{i\omega t - ikx} \left[\left(i\omega + f_g - ikv_g\right) \tilde{p}_g(\omega,k) - f_s\, \tilde{p}_s(\omega,k) \right]$$

$$0 = \int dk\, d\omega\, e^{i\omega t - ikx} \left[\left(i\omega + f_s + ikv_s\right) \tilde{p}_s(\omega,k) - f_g\, \tilde{p}_g(\omega,k) \right]$$

Which can be written as a matrix equation:

$$0 = \begin{pmatrix} i\omega + f_g - ikv_g & -f_s \\ -f_g & i\omega + f_s + ikv_s \end{pmatrix} \begin{pmatrix} \tilde{p}_g(\omega,k) \\ \tilde{p}_s(\omega,k) \end{pmatrix}$$

This equation only has non-zero solutions for $\tilde{p}_g$ and $\tilde{p}_s$ if the matrix determinant is equal to zero:

$$0 = det \begin{pmatrix} i\omega + f_g - ikv_g & -f_s \\ -f_g & i\omega + f_s + ikv_s \end{pmatrix} = \left(i\omega + f_g - ikv_g\right)\left(i\omega + f_s + ikv_s\right) + f_g\, f_s$$

This equation can be written as a dispersion relation:

$$\omega(k) = \overbrace{\left(\frac{f_s}{f_s + f_g} v_g - \frac{f_g}{f_s + f_g} v_s\right)}^{=\bar{v}} k + i \overbrace{\left(\frac{f_s\, f_g (v_g + v_s)^2}{(f_g + f_s)^3}\right)}^{=\bar{D}} k^2 + O(k^3) = \bar{v}\, k + i\, \bar{D}\, k^2 + O(k^3)$$

For large times t both ω and k are small so that we can drop terms of the order of k^3. The dispersion relation is then the same as for a diffusion advection process with drift velocity $\bar{v}$ and Diffusion coefficient $\bar{D}$. For $\bar{v} > 0$ the system will evolve like a diffusion advection process in

bioRxiv preprint doi: https://doi.org/10.1101/2021.06.03.446862; this version posted August 6, 2021. The copyright holder for this preprint (which was not certified by peer review) is the author/funder, who has granted bioRxiv a license to display the preprint in perpetuity. It is made available under aCC-BY-NC 4.0 International license.

which microtubules would have no average length so that they will become as long as the system allows, i.e. their growth is "unbounded".

For $\bar{v} < 0$, microtubules will exhibit an average length that depends on their dynamic parameters which can be calculated as follows: For large times, the overall probability to find a microtubule with length l at time t ($p(l,t) = p_g(l,t) + p_s(l,t)$) can be approximated by a modified diffusion-advection equation:

$$\frac{\partial}{\partial t} p(l,t) = \bar{D} \frac{\partial^2}{\partial l^2} p(l,t) + |\bar{v}| \frac{\partial}{\partial l} p(l,t)$$

The stationary state $\frac{\partial}{\partial t} p(l,t) = 0$ is thus found by:

$$0 = \frac{\partial^2}{\partial l^2} p(l) + \frac{|\bar{v}|}{\bar{D}} \frac{\partial}{\partial l} p(l)$$

The general solution to this partial differential equation is:

$$p(l) = C_1 \frac{\bar{D}}{|\bar{v}|} e^{-\frac{\bar{v}}{\bar{D}} l} + C_2$$

For $p(l,t)$ to be normalisable: $C_2 = 0$ and $C_1 = \left(\frac{|\bar{v}|}{\bar{D}}\right)^2$. So that:

$$p(l) = \frac{|\bar{v}|}{\bar{D}} e^{-\frac{\bar{v}}{\bar{D}} l}$$

Finally, one can calculate the average microtubule length l_{MT} as the expectation value of the length:

bioRxiv preprint doi: https://doi.org/10.1101/2021.06.03.446862; this version posted August 6, 2021. The copyright holder for this preprint (which was not certified by peer review) is the author/funder, who has granted bioRxiv a license to display the preprint in perpetuity. It is made available under aCC-BY-NC 4.0 International license.

$$l_{MT} \equiv \langle l \rangle = \int_0^\infty dl \; l \, p(l) = \frac{\bar{D}}{|\bar{v}|} = \frac{f_s \, f_g (v_g + v_s)^2}{\left(f_g + f_s\right)^2 (v_s f_g - v_g f_s)}$$

For $v_s/v_g \approx 1$, $f_s/f_g \approx 1$, and $d = v/f$ the quadratic terms can be Taylor expanded to yield:

$$l_{MT} \approx \frac{v_g v_s}{\left(v_s f_g - v_g f_s\right)} = \frac{d_g d_s}{d_s - d_g}$$

Analytical model to estimate microtubule growth per cycle based on immunostainings

The p150 fluorescence profile were calculated as described in the section on "p150 antibody staining". Subsequently, an exponential function, $p150(x) = b + e^{-s(x-x_0)}$, was fitted to the first 12 bins of the data (corresponds to up until 120 µm from the tip). Next, we assumed that $d_g(x) = A \, p150(x)^\alpha$, i.e. microtubule growth per cycle is a simple power law in the p150 fluorescence intensity. Thereby the expected growth length per cycle for a microtubule that starts growing at position x towards (1) or away (-1) from the cell body becomes:

$$d_g(x, sign) = 0.5 \left(d_g\left(sign \, d_g(x) + x\right) + d_g(x) \right)$$

This function was subsequently fitted to the growth length data presented in **FIGURE 1F.** To do so, the experimental data was first binned in bins of size 10 µm (like the staining data). Then we calculated the integral of $d_g(x, sign)$ over each bin for each direction of growth and minimised the squared difference to the experimental results by varying A and α. Note that we assumed that microtubules that grow way from the tip have to be at least 4 µm away from it (average microtubule length (Yu and Baas, 1994)) and that microtubules that grow into the tip may penetrate it by 2 µm.

bioRxiv preprint doi: https://doi.org/10.1101/2021.06.03.446862; this version posted August 6, 2021. The copyright holder for this preprint (which was not certified by peer review) is the author/funder, who has granted bioRxiv a license to display the preprint in perpetuity. It is made available under aCC-BY-NC 4.0 International license.

Microtubule sliding simulations

Details of the simulation can be found in (Jakobs et al., 2020). We here present a brief description that focusses on the novel way in which new microtubules are added during the simulation. Microtubules were arranged with their long axis along the *x*-axis of a Cartesian coordinate system and their centers on a hexagonal lattice in the $y - z$ plane. For simplicity all microtubules were assumed to have the same length, l_{MT} = 4µm. The inter-MT spacing in the y - z plane (~ 30 nm) was assumed to allow individual molecular motors (here, cytoplasmic dynein) to intervene between adjacent filaments and cross-link them with their respective 'cargo' or 'walking' domains. The simulation was initialized with 10 randomly oriented microtubules that were randomly distributed on a hexagonal lattice of lenght 6 µm. New microtubules were added to the system depending on the chosen nucleation model:

1. Sliding only: Microtubules were added at random locations with random orientation every 1100 seconds (~18 minutes). The time was optimised to yield axons of approximately the same length as cultured ones.
2. Sliding and templating: Microtubules were added at random locations every 1100 seconds. The likelihood of being +end out was calculated by counting the number and orientation of microtubules at the location (the center of the microtubule) in which the microtubule is added. Then the number of +end out microtubules was divided by the total number of microtubules to calculate the probability of getting a +end out microtubule. Finally a random number is drawn between 0 and 1 to determine the orientation of the added microtubule.

bioRxiv preprint doi: https://doi.org/10.1101/2021.06.03.446862; this version posted August 6, 2021. The copyright holder for this preprint (which was not certified by peer review) is the author/funder, who has granted bioRxiv a license to display the preprint in perpetuity. It is made available under aCC-BY-NC 4.0 International license.

3. Sliding and unbounded growth: A random location along the axon was chosen and a random microtubule orientation (50/50 +end out/-end out) introduced every 435 seconds. As not every microtubule nucleated in this model, the rate of influx was selected to be higher to enable the same axon growth behaviour. Subsequently, we calculated the likelihood of exhibiting unbounded growth for a microtubule with the randomly selected orientation and location. To do so, we first calculated the average added length per growth cycle in 10µm bins (distance from the axon tip and separately for +end out and -end out microtubules) for each axon in the dataset presented in **FIGURE 1A-G**. For each bin we then queried whether growth was bounded (added length below 2.2µm) or unbounded. The likelihood of unbounded growth was calculated for each bin by counting the number of axons that exhibited unbounded growth in the bin and dividing that number by all axons. Subsequently, two exponential functions were fitted to the +end out and -end out microtubule data respectively to determine a function that gives the likelihood of unbounded growth for +end out and -end out microtubules as a function of distance from the axon tip. Finally, the random location and the predetermined orientation were used to look up the likelihood of unbounded growth and the microtubule was assumed to have nucleated successfully when a randomly drawn number [0,1] was smaller than that likelihood.
4. Sliding, templating and unbounded growth: A random location along the axon was chosen every 435 seconds and its orientation likelihood calculated as in 2. Subsequently, the unbounded growth likelihood was calculated as in 3. Microtubules only successfully entered the system if exhibiting unbounded growth.

bioRxiv preprint doi: https://doi.org/10.1101/2021.06.03.446862; this version posted August 6, 2021. The copyright holder for this preprint (which was not certified by peer review) is the author/funder, who has granted bioRxiv a license to display the preprint in perpetuity. It is made available under aCC-BY-NC 4.0 International license.

Microtubules that were neighbours on the *y-z* plane and overlapping along the x-axis were crosslinked by cytoplasmic dynein. For simplicity and due to the tight packing of microtubules in the bundle, only motion in parallel to the *x*-axis was considered. Microtubule velocities were determined by solving a set of force balance equations that characterize dynein interaction with the microtubules, detailed in (Jakobs et al., 2020). Furthermore, the left boundary was a leaky spring; microtubules that moved into the left boundary were subject to a force of 50 pN/µm and were able to leave the axon with a fixed rate per microtubule (0.00024/sec). The rate was adjusted to lead to axons of 50 µm in length after approximately 24 hours simulation time. The right boundary was a constant force of 50 pN as described in (Jakobs et al., 2020). Axons were simulated for 50001 iterations (~28 hours) and all results averaged over 50 separate simulations. Simulation parameters were as follows:

Symbol	**Description**	**Value**	**Reasoning**
χ	Fraction of overlapping microtubules that are cross linked	1	We previously explored how changing χ affects microtubule sliding (Jakobs et al., 2020; 2015). In this manuscript we simply wanted to explore the effect of different microtubule addition models on microtubule orientation in which we fixed the value at 1.

bioRxiv preprint doi: https://doi.org/10.1101/2021.06.03.446862; this version posted August 6, 2021. The copyright holder for this preprint (which was not certified by peer review) is the author/funder, who has granted bioRxiv a license to display the preprint in perpetuity. It is made available under aCC-BY-NC 4.0 International license.

λ	Number of motors bound in an overlapping region [#/µm]	5	We quantified (by eye) the number of microtubule crosslinks in EM images of axons (Hirokawa et al., 2010) which was approximately 3 per 100 nm.
l_{MT}	Microtubule lengths [µm]	4 µm	Average microtubule lengths in axons measured in (Yu and Baas, 1994)
ξ	Drag coefficient of the axoplasm	1 pN sec / µm^2	Same coefficient used in (Oelz et al., 2018)
f_s	Dynein stall force	1.4 pN	Same coefficient used in (Oelz et al., 2018)
v_0	Dynein free velocity	0.86 µm/sec	Same coefficient used in (Oelz et al., 2018)
dt	Simulation timestep per iteration	2 seconds	As we showed previously (Jakobs et al., 2020; 2015), this value is a good choice to ensure smooth movements of microtubules during the simulation.

468

bioRxiv preprint doi: https://doi.org/10.1101/2021.06.03.446862; this version posted August 6, 2021. The copyright holder for this preprint (which was not certified by peer review) is the author/funder, who has granted bioRxiv a license to display the preprint in perpetuity. It is made available under aCC-BY-NC 4.0 International license.

Acknowledgements: We would like to thank Eva Pillai, Dennis Bray, Michael Takla, and Kevin Chalut for inspiring discussions and proofreading, Andreas Prokop and Cristina Melero for teaching *Drosophila* dissection techniques, and Sarah Bray, Dmitry Nashchekin, Daniel St Johnston, and Nick Brown for providing *Drosophila* strains and laboratory space to work in. The authors acknowledge funding from the Wellcome Trust (PhD studentship 109145/Z/15/Z to MAHJ), the UK Biotechnology and Biological Sciences Research Council (Research Grant BB/N006402/1 to KF), the European Research Council (Consolidator Award 772426 to KF), and the Alexander von Humboldt Foundation (Alexander von Humboldt Professorship to KF).

Competing interests: AZ declares no competing interests, MAHJ and KF are shareholders of deepMirror (https://deepmirror.ai), a company that, amongst other things, sells custom interfaces of the freeware *KymoButler*.

Supplementary Information:

Figures S1-S6

bioRxiv preprint doi: https://doi.org/10.1101/2021.06.03.446862; this version posted August 6, 2021. The copyright holder for this preprint (which was not certified by peer review) is the author/funder, who has granted bioRxiv a license to display the preprint in perpetuity. It is made available under aCC-BY-NC 4.0 International license.

References

Ahmad, F.J., Echeverri, C.J., Vallee, R.B., and Baas, P.W. (1998). Cytoplasmic dynein and dynactin are required for the transport of microtubules into the axon. J Cell Biol *140*, 391–401.

Baas, P.W., BLACK, M.M., and BANKER, G.A. (1989). Changes in microtubule polarity orientation during the development of hippocampal neurons in culture. J Cell Biol *109*, 3085–3094.

Bergstralh, D.T., Lovegrove, H.E., and St Johnston, D. (2015). Lateral adhesion drives reintegration of misplaced cells into epithelial monolayers. Nat Cell Biol *17*, 1497–1503.

Bray, D., Money, N.P., Harold, F.M., and Bamburg, J.R. (1991). Responses of growth cones to changes in osmolality of the surrounding medium. J Cell Sci *98 (Pt 4)*, 507–515.

Bulgakova, N.A., Grigoriev, I., Yap, A.S., Akhmanova, A., and Brown, N.H. (2013). Dynamic microtubules produce an asymmetric E-cadherin-Bazooka complex to maintain segment boundaries. J Cell Biol *201*, 887–901.

Bulgakova, N.A., Klapholz, B., and Brown, N.H. (2012). Cell adhesion in Drosophila: versatility of cadherin and integrin complexes during development. Current Opinion in Cell Biology *24*, 702–712.

del Castillo, U., Winding, M., Lu, W., Gelfand, V.I., and Allan, V. (2015). Interplay between kinesin-1 and cortical dynein during axonal outgrowth and microtubule organization in Drosophila neurons. eLife Sciences *4*, e10140.

Dogterom, M., and Leibler, S. (1993). Physical aspects of the growth and regulation of microtubule structures. Phys. Rev. Lett. *70*, 1347–1350.

Egger, B., van Giesen, L., Moraru, M., and Sprecher, S.G. (2013). In vitro imaging of primary neural cell culture from Drosophila. Nat Protoc *8*, 958–965.

Eng, H., Lund, K., and Campenot, R.B. (1999). Synthesis of beta-tubulin, actin, and other proteins in axons of sympathetic neurons in compartmented cultures. Journal of Neuroscience *19*, 1–9.

Franze, K. (2020). Integrating Chemistry and Mechanics: The Forces Driving Axon Growth. Annu. Rev. Cell Dev. Biol. *36*, 61–83.

Fukata, Y., Itoh, T.J., Kimura, T., Ménager, C., Nishimura, T., Shiromizu, T., Watanabe, H., Inagaki, N., Iwamatsu, A., Hotani, H., et al. (2002). CRMP-2 binds to tubulin heterodimers to promote microtubule assembly. Nat Cell Biol *4*, 583–591.

Gill, S.R., Schroer, T.A., Szilak, I., Steuer, E.R., Sheetz, M.P., and Cleveland, D.W. (1991). Dynactin, a conserved, ubiquitously expressed component of an activator of vesicle motility mediated by cytoplasmic dynein. J Cell Biol *115*, 1639–1650.

Heidemann, S.R., Landers, J.M., and Hamborg, M.A. (1981). Polarity orientation of axonal microtubules. J Cell Biol *91*, 661–665.

Hirokawa, N., Niwa, S., and Tanaka, Y. (2010). Molecular Motors in Neurons: Transport Mechanisms and Roles in Brain Function, Development, and Disease. Neuron *68*, 610–638.

Inagaki, N., Chihara, K., Arimura, N., Ménager, C., Kawano, Y., Matsuo, N., Nishimura, T., Amano, M., and Kaibuchi, K. (2001). CRMP-2 induces axons in cultured hippocampal neurons. Nat. Neurosci. *4*, 781–782.

bioRxiv preprint doi: https://doi.org/10.1101/2021.06.03.446862; this version posted August 6, 2021. The copyright holder for this preprint (which was not certified by peer review) is the author/funder, who has granted bioRxiv a license to display the preprint in perpetuity. It is made available under aCC-BY-NC 4.0 International license.

Jakobs, M.A.H., Franze, K., and Zemel, A. (2020). Mechanical Regulation of Neurite Polarization and Growth: A Computational Study. Biophysical Journal *118*, 1914–1920.

Jakobs, M.A., Dimitracopoulos, A., and Franze, K. (2019). KymoButler, a deep learning software for automated kymograph analysis. eLife Sciences *8*, 168.

Jakobs, M., Franze, K., and Zemel, A. (2015). Force Generation by Molecular-Motor-Powered Microtubule Bundles; Implications for Neuronal Polarization and Growth. Front Cell Neurosci *9*, 441.

Kuijpers, M., and Hoogenraad, C.C. (2011). Centrosomes, microtubules and neuronal development. Mol. Cell. Neurosci. *48*, 349–358.

Lazarus, J.E., Moughamian, A.J., Tokito, M.K., and Holzbaur, E.L.F. (2013). Dynactin subunit p150(Glued) is a neuron-specific anti-catastrophe factor. PLoS Biol. *11*, e1001611.

Liang, X., Kokes, M., Fetter, R.D., Sallee, M.D., Moore, A.W., Feldman, J.L., and Shen, K. (2020). Growth cone-localized microtubule organizing center establishes microtubule orientation in dendrites. eLife Sciences *9*, 308.

Lowery, L.A., and Van Vactor, D. (2009). The trip of the tip: understanding the growth cone machinery. Nat. Rev. Mol. Cell Biol. *10*, 332–343.

Mattie, F.J., Stackpole, M.M., Stone, M.C., Clippard, J.R., Rudnick, D.A., Qiu, Y., Tao, J., Allender, D.L., Parmar, M., and Rolls, M.M. (2010). Directed microtubule growth, +TIPs, and kinesin-2 are required for uniform microtubule polarity in dendrites. Curr. Biol. *20*, 2169–2177.

Millecamps, S., and Julien, J.-P. (2013). Axonal transport deficits and neurodegenerative diseases. Nature Publishing Group *14*, 161–176.

Molines, A.T., Lemière, J., Edrington, C.H., Hsu, C.-T., Steinmark, I.E., Suhling, K., Goshima, G., Holt, L.J., Brouhard, G.J., and Chang, F. (2020). Physical properties of the cytoplasm modulate the rates of microtubule growth and shrinkage. bioRxiv *265*, 2020.10.27.352716.

Moughamian, A.J., and Holzbaur, E.L.F. (2012). Dynactin is required for transport initiation from the distal axon. Neuron *74*, 331–343.

Mukherjee, A., Jenkins, B., Fang, C., Radke, R.J., Banker, G., and Roysam, B. (2011). Automated kymograph analysis for profiling axonal transport of secretory granules. Medical Image Analysis *15*, 354–367.

Mukherjee, A., Brooks, P.S., Bernard, F., Guichet, A., and Conduit, P.T. (2020). Microtubules originate asymmetrically at the somatic golgi and are guided via Kinesin2 to maintain polarity within neurons. eLife Sciences *9*, 2191.

Nguyen, M.M., McCracken, C.J., Milner, E.S., Goetschius, D.J., Weiner, A.T., Long, M.K., Michael, N.L., Munro, S., and Rolls, M.M. (2014). Γ-tubulin controls neuronal microtubule polarity independently of Golgi outposts. Mol. Biol. Cell *25*, 2039–2050.

Nieuwburg, R., Nashchekin, D., Jakobs, M., Carter, A.P., Khuc Trong, P., Goldstein, R.E., and St Johnston, D. (2017). Localised dynactin protects growing microtubules to deliver oskar mRNA to the posterior cortex of the Drosophila oocyte. eLife Sciences *6*, 711.

Oelz, D.B., del Castillo, U., Gelfand, V.I., and Mogilner, A. (2018). Microtubule Dynamics, Kinesin-1 Sliding, and Dynein Action Drive Growth of Cell Processes. Biophysical Journal *115*, 1614–1624.

bioRxiv preprint doi: https://doi.org/10.1101/2021.06.03.446862; this version posted August 6, 2021. The copyright holder for this preprint (which was not certified by peer review) is the author/funder, who has granted bioRxiv a license to display the preprint in perpetuity. It is made available under aCC-BY-NC 4.0 International license.

Plough, H.H., and Ives, P.T. (1935). Induction of Mutations by High Temperature in Drosophila. Genetics *20*, 42–69.

Pool, M., Thiemann, J., Bar-Or, A., and Fournier, A.E. (2008). NeuriteTracer: a novel ImageJ plugin for automated quantification of neurite outgrowth. Journal of Neuroscience Methods *168*, 134–139.

Rao, A.N., Patil, A., Black, M.M., Craig, E.M., Myers, K.A., Yeung, H.T., and Baas, P.W. (2017). Cytoplasmic Dynein Transports Axonal Microtubules in a Polarity-Sorting Manner. Cell Rep *19*, 2210–2219.

Sanchez-Soriano, N., Gonçalves Pimentel, C., Beaven, R., Haessler, U., Ofner Ziegenfuss, L., Ballestrem, C., and Prokop, A. (2010). Drosophila growth cones: A genetically tractable platform for the analysis of axonal growth dynamics. Developmental Neurobiology *70*, 58–71.

Sánchez-Huertas, C., Freixo, F., Viais, R., Lacasa, C., Soriano, E., and Lüders, J. (2016). Non-centrosomal nucleation mediated by augmin organizes microtubules in post-mitotic neurons and controls axonal microtubule polarity. Nat Commun *7*.

Schindelin, J., Arganda-Carreras, I., Frise, E., Kaynig, V., Longair, M., Pietzsch, T., Preibisch, S., Rueden, C., Saalfeld, S., Schmid, B., et al. (2012). Fiji: an open-source platform for biological-image analysis. Nat. Methods *9*, 676–682.

Seetapun, D., and Odde, D.J. (2010). Cell-length-dependent microtubule accumulation during polarization. Curr. Biol. *20*, 979–988.

Shimada, Y., Yonemura, S., Ohkura, H., Strutt, D., and Uemura, T. (2006). Polarized Transport of Frizzled along the Planar Microtubule Arrays in Drosophila Wing Epithelium. Dev. Cell *10*, 209–222.

Stepanova, T., Slemmer, J., Hoogenraad, C.C., Lansbergen, G., Dortland, B., De Zeeuw, C.I., Grosveld, F., van Cappellen, G., Akhmanova, A., and Galjart, N. (2003). Visualization of microtubule growth in cultured neurons via the use of EB3-GFP (end-binding protein 3-green fluorescent protein). J. Neurosci. *23*, 2655–2664.

Stone, M.C., Roegiers, F., and Rolls, M.M. (2008). Microtubules have opposite orientation in axons and dendrites of Drosophila neurons. Mol. Biol. Cell *19*, 4122–4129.

Tas, R.P., Chazeau, A., Cloin, B.M.C., Lambers, M.L.A., Hoogenraad, C.C., and Kapitein, L.C. (2017). Differentiation between Oppositely Oriented Microtubules Controls Polarized Neuronal Transport. Neuron *96*, 1264–1271.e1265.

Twelvetrees, A.E., Pernigo, S., Sanger, A., Guedes-Dias, P., Schiavo, G., Steiner, R.A., Dodding, M.P., and Holzbaur, E.L.F. (2016). The Dynamic Localization of Cytoplasmic Dynein in Neurons Is Driven by Kinesin-1. Neuron *90*, 1000–1015.

van Beuningen, S.F.B., Will, L., Harterink, M., Chazeau, A., van Battum, E.Y., Frias, C.P., Franker, M.A.M., Katrukha, E.A., Stucchi, R., Vocking, K., et al. (2015). TRIM46 Controls Neuronal Polarity and Axon Specification by Driving the Formation of Parallel Microtubule Arrays. Neuron *88*, 1208–1226.

Vasquez, R.J., Howell, B., Yvon, A.M., Wadsworth, P., and Cassimeris, L. (2017). Nanomolar concentrations of nocodazole alter microtubule dynamic instability in vivo and in vitro. Mol. Biol. Cell *8*, 973–985.

Waterman-Storer, C.M., Karki, S.B., Kuznetsov, S.A., Tabb, J.S., Weiss, D.G., Langford, G.M., and Holzbaur, E.L. (1997). The interaction between cytoplasmic dynein and dynactin is required for fast axonal transport. Pnas *94*, 12180–12185.

Yannoni, Y.M., and White, K. (1997). Association of the neuron-specific RNA binding domain-containing protein ELAV with the coiled body in Drosophila neurons. Chromosoma *105*, 332–341.

bioRxiv preprint doi: https://doi.org/10.1101/2021.06.03.446862; this version posted August 6, 2021. The copyright holder for this preprint (which was not certified by peer review) is the author/funder, who has granted bioRxiv a license to display the preprint in perpetuity. It is made available under aCC-BY-NC 4.0 International license.

Yau, K.W., Schätzle, P., Tortosa, E., Pagès, S., Holtmaat, A., Kapitein, L.C., and Hoogenraad, C.C. (2016). Dendrites In Vitro and In Vivo Contain Microtubules of Opposite Polarity and Axon Formation Correlates with Uniform Plus-End-Out Microtubule Orientation. J. Neurosci. *36*, 1071–1085.

Yu, W., and Baas, P.W. (1994). Changes in microtubule number and length during axon differentiation. Journal of Neuroscience *14*, 2818–2829.

Yu, W., Qiang, L., Solowska, J.M., Karabay, A., Korulu, S., and Baas, P.W. (2008). The Microtubule-severing Proteins Spastin and Katanin Participate Differently in the Formation of Axonal Branches. Mol. Biol. Cell *19*, 1485–1498.

bioRxiv preprint doi: https://doi.org/10.1101/2021.06.03.446862; this version posted August 6, 2021. The copyright holder for this preprint (which was not certified by peer review) is the author/funder, who has granted bioRxiv a license to display the preprint in perpetuity. It is made available under aCC-BY-NC 4.0 International license.

Figures

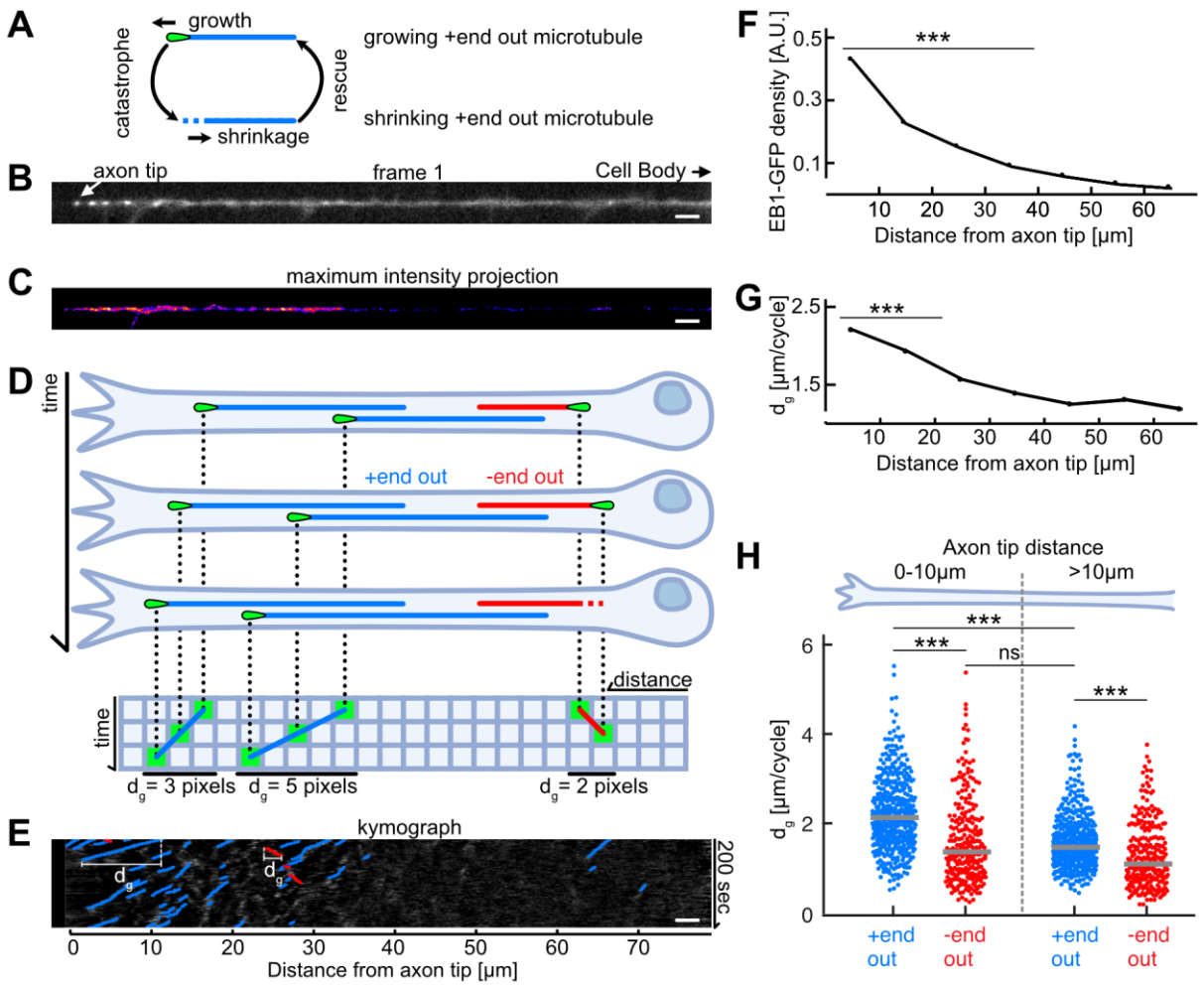

Figure 1: Axonal microtubule orientation and localization regulate microtubule growth. (A) Schematic depicting the microtubule growth and shrinkage cycle. Microtubules grow until they undergo a catastrophe, which initiates microtubule shrinkage and can start growing again after a rescue event. During growth (but not shrinkage) EB1 localizes to microtubule tips. **(B)** First frame of a live cell imaging movie of axonal EB1-GFP dynamics. Bright dots represent individual EB1-GFP puncta, which label growing microtubule +ends. **(C)** Maximum intensity projection of a 200 seconds long movie depicting EB1-GFP dynamics in a *D melanogaster* axon. EB1-GFP density is increased towards the tip. **(D)** Schematic showing how EB1-GFP live imaging movies were visualized and analyzed using kymographs. The growing tips of +end out microtubules (blue) and -end out microtubules (red) were fluorescently labelled with EB1-GFP (green tear drop shaped 'comets'). The same axon is shown at three different time points;

bioRxiv preprint doi: https://doi.org/10.1101/2021.06.03.446862; this version posted August 6, 2021. The copyright holder for this preprint (which was not certified by peer review) is the author/funder, who has granted bioRxiv a license to display the preprint in perpetuity. It is made available under aCC-BY-NC 4.0 International license.

microtubules grow at their +end, where EB1-GFP is located. The axonal intensity profiles of all time points are plotted underneath each other, resulting in a space-time grid called 'kymograph'. Connecting puncta between consecutive kymograph lines with blue/red lines yields the overall displacement d_g for individual microtubule growth events. Note that the red -end out microtubule stops growing in the 2nd frame and shrinks in the 3rd frame **(E)** Kymograph showing EB1-GFP dynamics analyzed with *KymoButler* (Jakobs et al., 2019). Lines with a positive slope (blue, left to right upwards) are microtubules growing with their +end towards the axon tip, lines with negative slope (red, left to right downwards) are microtubules growing away from the tip. Horizontal bars indicate the growth lengths (d_g) for individual microtubule growth cycles. **(F)** EB1-GFP comet density as a function of the distance from the axon tip. Most microtubule polymerization occurred near the advancing axon tip. (N = 346, 20 biological replicates, $p < 10^{-20,}$ Kruskal Wallis test, $p < 10^{-7}$ for pairwise comparisons between bin 1-4, Dunn-Sidak post hoc test). **(G)** Microtubule added length per cycle d_g as a function of distance from the axon tip. Microtubules grew longer in the vicinity of the axon tip ($p < 10^{-20}$, Kruskal Wallis test, $p < 10^{-7}$ for pairwise comparisons of either bin 1 or 2 with any other bin, Dunn-Sidak post hoc test). **(H)** d_g for +end out (blue) and -end out (red) microtubules grouped for growth in the distalmost 10 µm of the axon tip, and further away than 10 µm from the axon tip. Each dot represents the average of one axon in the respective region, grey lines indicate median values. With d_g = 2.24 ± 0.00 µm / cycle (mean ± SEM), +end out microtubules near the axon tip grew significantly longer than -end out microtubules (d_g = 1.68 ± 0.00 µm / cycle) and microtubules located further away from the tip (N = 346 axons, 20 biological replicates; $p < 10^{-30}$, Kruskal Wallis test followed by Dunn-Sidak post hoc test; *** $p < 10^{-4}$). Scale bars: 3µm.

bioRxiv preprint doi: https://doi.org/10.1101/2021.06.03.446862; this version posted August 6, 2021. The copyright holder for this preprint (which was not certified by peer review) is the author/funder, who has granted bioRxiv a license to display the preprint in perpetuity. It is made available under aCC-BY-NC 4.0 International license.

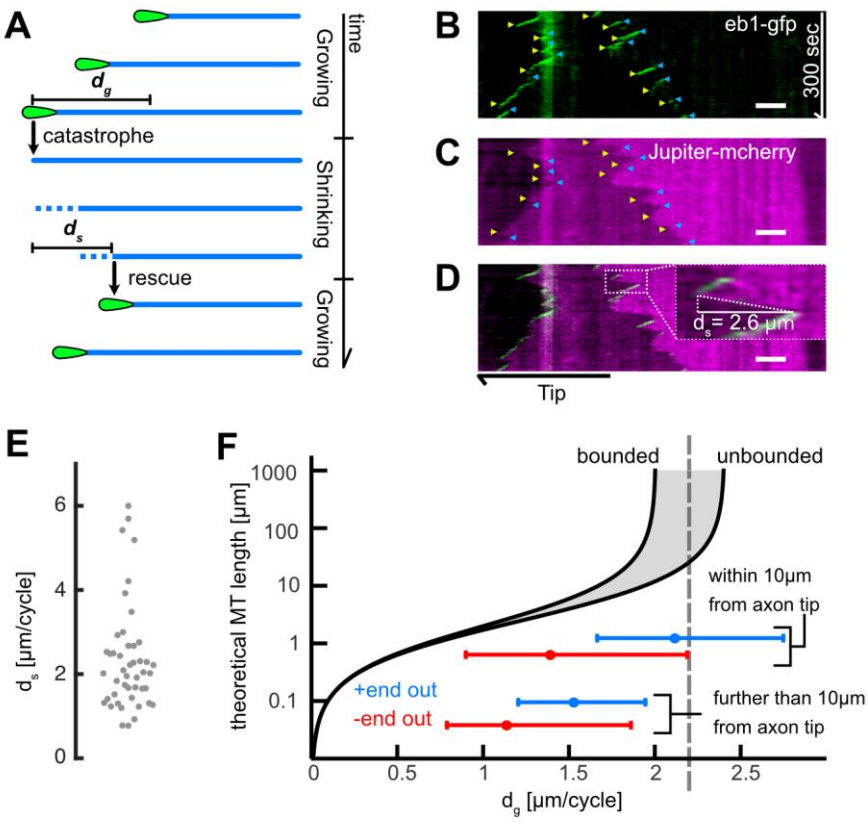

Figure 2: Microtubule length depends on growth length per cycle. (**A)** Schematic highlighting the assumptions of our two-state master equation model. Microtubules were assumed to occupy either a growing or shrinking state. During a growth cycle, the average microtubule length increases by d_g , during a shrinkage cycle, microtubule length decreases by d_s . Additionally, microtubules were able to stochastically switch between the two states as shown in **Figure 1A. (B-D)** Kymographs from a *D. melanogaster* axon that expressed **(B)** EB1-GFP (green) and **(C)** Jupiter-mCherry, a tubulin label (magenta). Individual microtubule shrinkage events, visible as **(C)** fluorescent edges and **(D)** dashed white lines in the kymograph, yielded microtubule shrinkage lengths per cycle d_s. Yellow and blue markers in **B** & **C** indicate start and end points of an individual shrinkage event and the inset in **D** highlights an individual shrinkage event. Scale bars: 3µm**. (E)** Average d_s values for N=47 axons (3 biological replicates; mean: 2.20±0.20 µm (± s.e.m). **(F)** A plot of the estimated overall microtubule length l_{MT} as a function of d_g with d_s = 2.20±0.20 µm. The two solid black lines indicate the lower and upper bounds of the average microtubule lengths for a given d_g with d_s = 2.0 or 2.4 µm. One can separate two regimes; "unbounded" and "bounded" growth, separated by a dashed line. Blue and red horizontal lines represent median ± lower and upper quantiles for +end out and -end out microtubules,

bioRxiv preprint doi: https://doi.org/10.1101/2021.06.03.446862; this version posted August 6, 2021. The copyright holder for this preprint (which was not certified by peer review) is the author/funder, who has granted bioRxiv a license to display the preprint in perpetuity. It is made available under aCC-BY-NC 4.0 International license.

respectively. The top two lines represent microtubules found at the distalmost 10 µm of the axon, the bottom lines microtubules found further than 10 µm away. +end out microtubules close to the tip were considerably more likely to exhibit unbounded growth than +end out microtubules further away from the tip and -end out microtubules.

bioRxiv preprint doi: https://doi.org/10.1101/2021.06.03.446862; this version posted August 6, 2021. The copyright holder for this preprint (which was not certified by peer review) is the author/funder, who has granted bioRxiv a license to display the preprint in perpetuity. It is made available under aCC-BY-NC 4.0 International license.

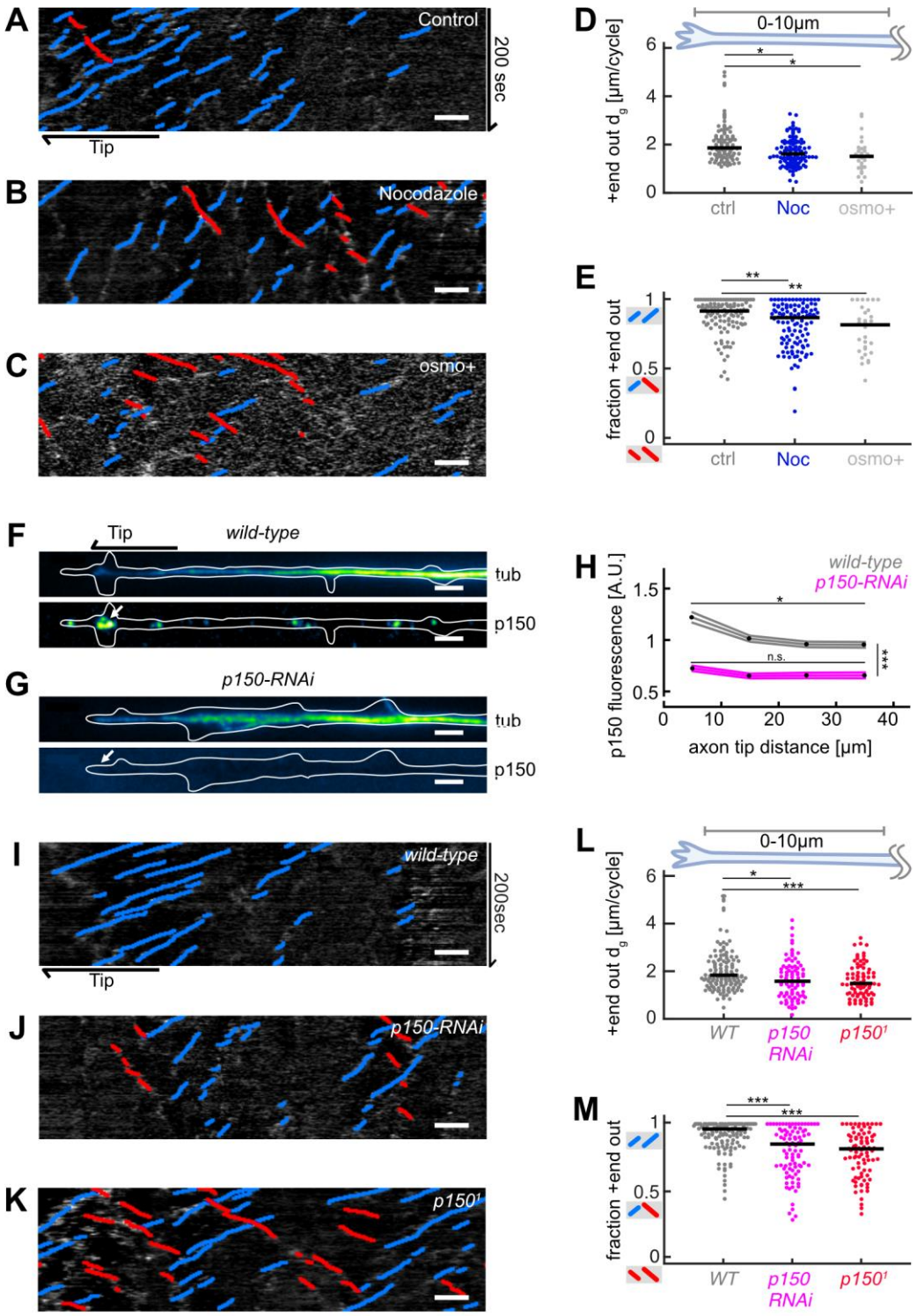

644

645 **Figure 3: Decreased microtubule growth decreases axonal microtubule orientation. (A-C)** Representative

646 kymographs analyzed with *KymoButler* (Jakobs et al., 2019) from axonal processes treated with (**A**) 0.025% DMSO

bioRxiv preprint doi: https://doi.org/10.1101/2021.06.03.446862; this version posted August 6, 2021. The copyright holder for this preprint (which was not certified by peer review) is the author/funder, who has granted bioRxiv a license to display the preprint in perpetuity. It is made available under aCC-BY-NC 4.0 International license.

(control) for 8h, **(B)** 5uM Nocodazole for 8h, **(C)** medium with increased osmolarity ("osmo+") for 22h. Growth of +end out microtubules is shown as blue lines, -end microtubules are red. Scale bars = 3µm. **(D)** Added growth lengths per cycle d_g of +end out microtubules at the distalmost 10µm from the axon tip for control (N = 107 axons from 5 biological replicates), nocodazole-treated axons (N = 116 axons from 3 biological replicates), and axons cultured in osmo+ medium (N = 30, 2 biological replicates). Microtubule lengths increased significantly less per growth cycle in axons treated with Nocodazole or osmo+ media than controls ($p < 10^{-4}$, Kruskal Wallis test, * $p < 0.05$ for pairwise comparisons, Dunn-Sidak post hoc test). **(E)** The fraction of +end out microtubules, in the different groups. Microtubule orientation was calculated by counting all microtubules that grew away from the cell body (blue lines in kymographs) and dividing them by all growing microtubules (blue and red). This way, a kymograph with only blue lines gives a value of 1 while an equal number of blue and red lines yields a value of 0.5. Microtubules in axons treated with Nocodazole or osmo+ media were significantly less uniformly oriented than those in the control group, i.e., they contained a larger fraction of microtubules pointing with their +ends toward the cell body (red lines in **(A-C)**) ($p < 10^{-4}$, Kruskal Wallis test, ** $p < 10^{-2}$ for pairwise comparisons, Dunn-Sidak post hoc test). **(F-G)** Tubulin (top) and normalized p150 (bottom) immunostaining of cultured *D. melanogaster* larvae axonal processes of **(F)** controls and **(G)** neurons expressing *elav-gal4* UAS driven *p150-RNAi*. Large p150 puncta were found clustered around the axon tip (arrow) in controls **(F)** but not in *p150-RNAi* axons **(G)**. Scale bars = 2µm **(H)** Normalized p150 fluorescence intensity as a function of distance from the axon tip for *wild-type* axons (N = 33) and *p150-RNAi* axons (N = 32, 2 biological replicates). Lines represent mean ± s.e.m. for *wild-type* (grey) and *p150-RNAi* (magenta). P150 fluorescence intensities changed along the axon ($p < 10^{-70}$; Kruskal Wallis test). In *wild-type* axons, p150 was enriched at the axon tip (* $p < 0.05$ between bin 1 and bin 3 or 4; pairwise comparisons with Dunn-Sidak post hoc test), but not in *p150-RNAi* expressing axons ($p > 0.05$ for all pairwise comparisons). Overall, p150 expression levels were diminished in *p150-RNAi* axons compared to *wild-type* (*** $p < 10^{-7}$ for any pairwise comparison between conditions). **(I-K)** *KymoButler* output for kymographs of EB1-GFP expressed in (**I**) a *wild-type* axon, **(J)** an axon expressing p150-RNAi, and **(K)** an axon in a $p150^1/+$ mutant background. Scale bars = 3 µm. Blue/red lines represent microtubules with +/-end out orientation, respectively. **(L)** +end out microtubule added length per cycle d_g for *wild-type* (N = 85, 9 biological replicates), *p150-RNAi* (N = 34, 3 biological replicates), and $p150^1/+$ (N = 83, 6 biological replicates). Microtubule growth lengths were significantly decreased in both *p150-RNAi* and $p150^1$ conditions compared to

bioRxiv preprint doi: https://doi.org/10.1101/2021.06.03.446862; this version posted August 6, 2021. The copyright holder for this preprint (which was not certified by peer review) is the author/funder, who has granted bioRxiv a license to display the preprint in perpetuity. It is made available under aCC-BY-NC 4.0 International license.

controls ($p < 10^{-9}$, Kruskal Wallis test, **$p < 0.001$, *$p < 0.05$, Dunn-Sidak post hoc test). **(M)** Microtubule orientation for *wild-type*, *p150-RNAi*, and *p150^{1}/+*. Microtubules were less uniformly oriented in both *p150-RNAi* and *p150^{1}* axons ($p < 10^{-9}$, Kruskal Wallis test, *** $p < 10^{-5}$ for pairwise comparisons with Dunn-Sidak post hoc test). Overall, axonal microtubule orientation was decreased after chemical, physical, and genetic perturbations of microtubule growth.

bioRxiv preprint doi: https://doi.org/10.1101/2021.06.03.446862; this version posted August 6, 2021. The copyright holder for this preprint (which was not certified by peer review) is the author/funder, who has granted bioRxiv a license to display the preprint in perpetuity. It is made available under aCC-BY-NC 4.0 International license.

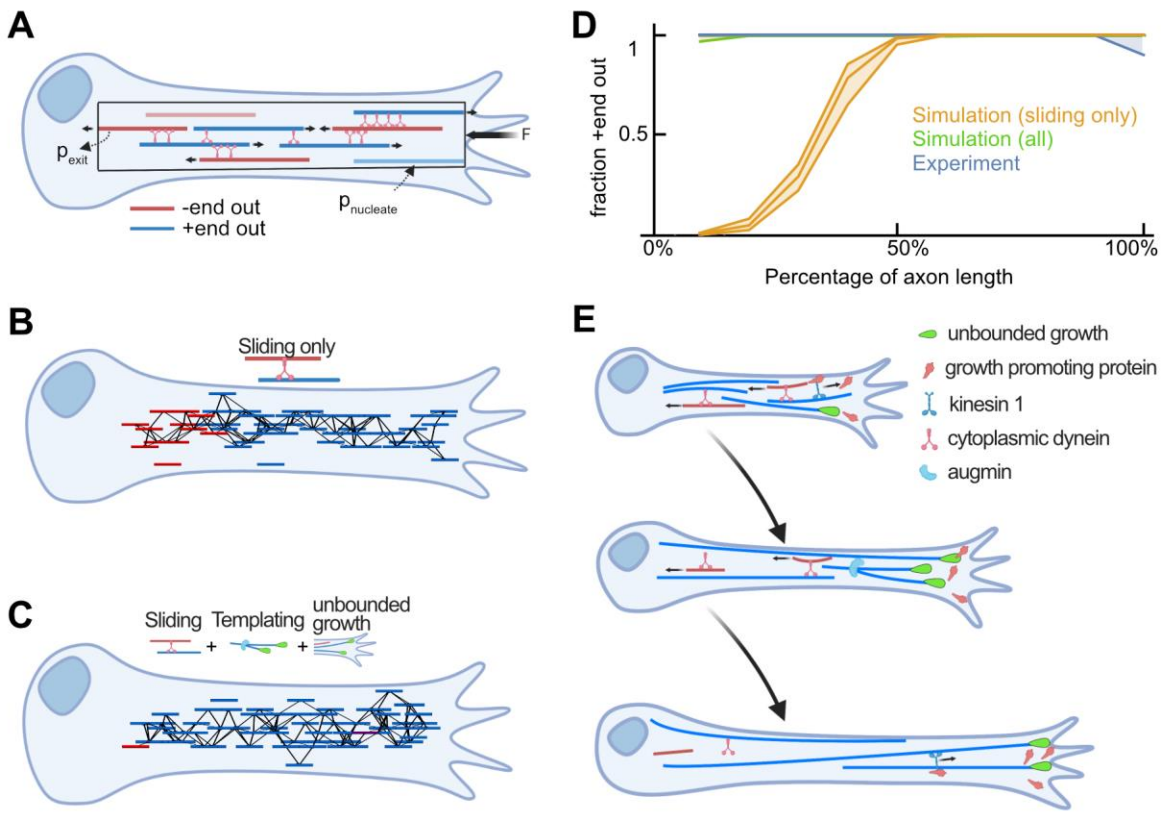

Figure 4: Unbounded microtubule growth into the advancing axon tip is required to establish axonal microtubule orientation. (A) Schematic showing the microtubule sliding simulation and its relevant parameters. **(B-D)** Simulation of microtubule dynamics. **(B)** Snapshot of a simulated axon with dynein-based sliding of microtubules. -end out microtubules accumulated within the proximal axon. **(C)** Snapshot of an axon simulated with sliding, augmin templating (new microtubules were likely oriented into the same direction as their surrounding ones), and higher likelihood of unbounded growth for +end out microtubules. Much like in real axons, most microtubules were oriented with their +end out throughout the axon. **(D)** Microtubule orientation along the normalized axon length for the simulations with sliding only (orange trace), with sliding, templating, and unbonded growth (green), and our experimental data (blue). Lines represent 30% to 70% quantiles. There was excellent agreement between the experimental and *in silico data.* **(E)** Summary of proposed mechanism for establishing microtubule orientation in axons. Red and blue lines represent -end out and +end out microtubules, respectively. Green drop shapes indicate unbounded microtubule growth into the axon tip for +end out microtubules. Kinesin 1 deposits microtubule growth

bioRxiv preprint doi: https://doi.org/10.1101/2021.06.03.446862; this version posted August 6, 2021. The copyright holder for this preprint (which was not certified by peer review) is the author/funder, who has granted bioRxiv a license to display the preprint in perpetuity. It is made available under aCC-BY-NC 4.0 International license.

promoting proteins, such as p150, at axon tips (**SUPPLEMENTARY FIGURE 4**), leading to local unbounded growth of +end out microtubules. Augmin templating and cell body-directed sliding of -end out microtubules further amplifies this bias. All three mechanisms together lead to a +end out microtubule cytoskeleton.